Melting and Crystallization of Differently Oriented Sets of Crystallites in Hard-Elastic Polypropylene

Norbert Stribeck[1 1]**, Ulrich Nöchel**[1]**, Stoyko Fakirov**[2]**, Sérgio S. Funari**[2]

[1]*Institute of Technical and Macromolecular Chemistry, University of Hamburg, Bundesstr. 45, 20146 Hamburg, Germany* [2]*HASYLAB at DESY, Notkestr. 85, 22603 Hamburg, Germany*

ABSTRACT: Uniaxially oriented polypropylene (PP) is molten and crystallized isothermally from the oriented, quiescent melt. Nucleation and growth of differently oriented sets of crystallites (*c*-set and a^*-set) appear decoupled. After shallow quench crystallization is preceded by (spinodal) decomposition. Evolution is monitored by wide-angle X-ray scattering (WAXS) and compared to results of a SAXS study. Peak integrals (crystallinity) and minimum crystallite size are tracked. In the commercial starting material a^*-set crystallites melt at 158°C. The *c*-set melts at 170°C furnace temperature. After recrystallization both sets melt at 170°C. Isothermal crystallization is divided in two distinct phases. During nucleation the crystallinity stays low. The second phase is dominated by crystallinity growth. At 150°C the *c*-set is seeded first. At 145°C and 140°C a^*-oriented crystallites are the first. The first-seeded set starts to grow first. *c*-set crystallinity is always growing faster than a^*-set crystallinity. The evolution of the SAXS cross-diagram in the growth phase can both be explained by lamellae growing at right angles, and by block merging.

1 Introduction

It is well-known[1] that uniaxially oriented polypropylene (PP) exhibits a bimodal crystallite orientation. In one of the two sets the unit-cell *c*-axis is parallel to the fiber axis. In the other set the a^*-axis is in fiber direction. The a^*-direction[2] is the normal on the *bc*-plane of the unit cell. During melt-spinning of PP first the wide-angle X-ray scattering (WAXS) reflections of the *c*-set crystallites appear[3] at the equator. Later the quasi-meridional reflections of the a^*-set show up. In the electron microscope a corresponding bimodal nanostructure has been discovered, the so-called *cross-hatched structure*.[4] It contains a second set of lamellae that are oriented transverse to the normal layers. They are containing a^*-oriented crystallites and are considered to be formed in a secondary process.[5,6]

Advance of X-ray scattering technique permits to investigate the crystallization of polymer materials with increasing precision and time-resolution. The established understanding concerning the relations among process parameters, mechanisms, and the resulting structure shall ultimately be exploited to tailor materials properties by optimization of the industrial processes. Nevertheless, if isotropic materials are studied, the information content of the scattering pattern is low, and simple models must be employed in the analysis. Studying the isothermal crystallization of PP from a quiescent, isotropic polypropylene melt Albrecht and Strobl[7] show that the isotropic small-angle X-ray scattering (SAXS) can only be fitted by a "stack of crystalline lamellae" in the first minutes after a shallow quench (i.e. high crystallization temperature). This scattering has as well been observed by the group of Ryan,[8,9] but has been related to a spinodal decomposition of the melt, because simultaneously no discrete WAXS has been observed. Other authors[10,11] observe simultaneous growth of discrete WAXS and SAXS. They conclude that a nucleation-and-growth process is dominating crystallization. In this context the question has been raised, if the detection limit[9,11,12] of common WAXS detectors were sufficient to capture the start of crystallite growth. In a very recent paper[13] the nucleation-and-growth mechanism has been affirmed by a crystallization study of isotropic PP in which the authors present data from a medium-deep quench to 145°C. They report that other experimental conditions give essentially the same results.

Thus, it appears suggestive to investigate crystallization at several crystallization temperatures, to use anisotropic samples (to avoid solid-angle smearing of discrete features), to record both SAXS and WAXS, and to elaborate a method that can be applied to anisotropic WAXS patterns and returns a well-founded measure of crystallinity. For this purpose we choose materials that crystallize in the uniaxially oriented state. Oriented crystallization of polymers can be achieved by cautiously melting highly oriented materials with fiber symmetry in order to preserve the orientation memory[14,15] of the polymer network, or by shearing[16–20] the melt. The indicated orientation-memory or self-nucleation effect has frequently been discussed,[21–24] and the memory has been attributed to bundles of extended chain segments that either are thought to be thin rigid "shish" crystallites or non-crystalline chain-bundles whose orientation persists on a time-scale on which chain entanglements do not move. With increasing melt-annealing temperature and time[15] the oriented quiescent melt turns into an isotropic quiescent melt. We say that we have started from an oriented quiescent melt, whenever oriented crystallites are emerging from a molten sample that does not show scat-

---

[1]Corresponding author. E-mail: norbert.stribeck@desy.de. Telephone: +49-40-42838-3615, Fax: +49-40-42838-6008

tering. Oriented quiescent melts have been observed[15] in polypropylene between 170°C (melt-annealing time $t_{ma} \geq$ 4 min) and 177°C ($t_{ma} \leq$4 min). These temperatures are far below the equilibrium melting temperature (212°C) of isotactic polypropylene.[25] Thus, in order either to indicate remnant crystallites or to determine the onset of crystallization, quantitative parameters that are proportional to crystallinity or to crystallite size are determined and plotted as a function of the elapsed time.

Two years ago we have published a time-resolved SAXS study on the crystallization mechanisms in oriented isotactic PP.[15] We have reported that after shallow quench (155°C and 150°C) the first discrete SAXS develops into meridional streaks. After medium and deep quench the first discrete SAXS patterns conform both to the model of a cross-hatched[4,5,7,26] lamellar structure, and to Strobl's block structure.[27,28] The ambiguity results from Babinet's theorem. Nevertheless, from the continued evolution of the scattering patterns into a pattern of oriented lamellae we have concluded that a merging of the blocks into lamellae is more probable than a disruption of cross-lamellae in a quiescent process.

Following the suggestions of the referees of our SAXS study,[15] we now, additionally, have monitored the isothermal crystallization of the same commercial material by WAXS. Here we present the results and discuss them in connection with the results of the SAXS study. In the course of the WAXS experiments several thousand two-dimensional (2D) WAXS patterns have been recorded. Data evaluation of such an amount of data can either be accomplished by a simple manual analysis method, or by automatic processing of the diffraction patterns. We have tested both possibilities. After one of us had deduced an exact equation for the determination of the fiber tilt angle,[29] an automatic quantitative evaluation procedure for fiber patterns[30] became possible. By means of this procedure one can easily track and compensate the tumbling of the fiber axis during the experiment. Moreover, materials parameters that are well-founded in scattering theory can be computed and tracked. Ultimately, we track the weight crystallinity and the extension of the crystallites for the two differently oriented sets of crystallites.

2 Experimental

Material. Commercial hard-elastic[31,32] polypropylene (HEPP) film (CelGard-PP®, Lot #884, as extruded by Hoechst-Celanese) of 25 µm thickness is studied. The films are produced[33] from the polypropylene (PP) grade Hercules Profax 6301 with a melt index 15.0(230°C) ASTM-D-1238. The weight-average molecular mass of the grade is $\overline{M}_w = 128000$ g/mol. The polydispersity of the material is $\overline{M}_w/\overline{M}_n = 4$. 16 sheets are stacked under consideration of their high uniaxial orientation, covered by aluminum foil (20 µm thickness), and fixed in a frame sample holder.

Figure 1: HEPP film after a melting and recrystallization experiment. Aluminum foils removed

WAXS Measurements. Wide-angle X-ray scattering is performed in the synchrotron beamline A2 at HASYLAB, Hamburg, Germany. The wavelength of the X-ray beam is 0.15 nm, and the sample-detector distance is 79 mm. Scattering patterns are collected by a two-dimensional position sensitive marccd 165 detector (mar research, Norderstedt, Germany) in binned 1024 × 1024 pixel mode (158.3 µm quadratic pixel size). During the experiments series of scattering patterns are recorded. The cycle-time is either 30 s (20 s exposure) or 8 s (4 s exposure), respectively.

Temperature Programs. The frames containing each a stack of foils are mounted in a furnace equipped with two heating cartridges and air cooling that is provided by HASYLAB. Hardware and temperature programs are the same as in a previous SAXS study.[15] The samples are rapidly heated to 150°C. Then the heating rate is lowered to 2°C/min in order to cautiously approach a melt-annealing temperature of 173°C. The melt-annealing temperature is kept for 4 min. After this time the sample is cooled to the crystallization temperature (either 150°C, 145°C, or 140°C) within 1 min. The temperature is measured in the sample holder. Thus, the sample temperature may be lower than the measured temperature. Figure 1 shows a sample after one of the experiments. The samples are warping during the experiments.

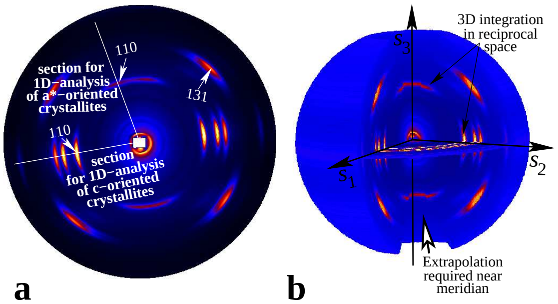

Figure 2: Variants of fiber diffraction analysis for hard-elastic polypropylene. (a) 1D analysis in the raw measured pattern by excision of curves and integration yielding integral and breadth of the 110-reflections. (b) 3D analysis by mapping the complete pattern into reciprocal space and 3D integration. s_1, s_2, and s_3 are the components of the scattering vector **s**

3 Data Analysis

All scattering patterns show the α_2-modification of polypropylene.[34] The WAXS data are analyzed in two different ways, which are sketched in Fig. 2. Figure 2a demonstrates a simple one-dimensional (1D) analysis that makes only rudimentary use of scattering theory. Figure 2b sketches a three-dimensional (3D) analysis method. Here the intensity of the fiber pattern (Fig. 2a) is mapped into reciprocal space, before peaks are isolated and analyzed by integration in reciprocal space. The change of color in the pseudo-color images from Fig. 2a to Fig. 2b indicates the intensity correction by consideration of the fiber mapping,[29,30] the absorption, and of the polarization factor. In principle, only the 3D evaluation is exact. Nevertheless, Fig. 2b reveals a general problem of fiber diffraction. A blind zone extends across the meridian (s_3-axis). It is a function of the fiber tilt angle β.

3.1 1D WAXS Trend Analysis

The 1D analysis ignores essential part of the scattering theory, in order to provide a trend analysis of the crystal structure evolution. As indicated in Fig. 2a, two scattering curves (sections) are cut from the raw diffraction patterns. The first cut runs along the equator passing the 3 strongest reflection peaks of PP. It serves the analysis of the c-oriented crystallites. The second cut runs through the maximum of the almost-meridional 110-reflection for an analysis of the crystallites whose a^*-axes are in fiber direction. As the orientation of the fiber axis with respect to the X-ray beam is tumbling during the experiment, the reflection maximum is moving on a circle.[29,35] It can even vanish at the meridian.

Without correction of the intensity the cuts are rescaled[2] from the detector coordinate system $\mathbf{p}$ to units of the scattering vector $\mathbf{s}$ in the direction of the cut. Thus, for the equatorial direction a curve $I_e(s_{12})$, and for the quasi-meridional direction $I_m(s_*)$ are obtained, respectively. Here $s = |\mathbf{s}| = (2/\lambda)\sin\theta$ is the modulus of the scattering vector, which is a function of the scattering angle 2θ and the X-ray wavelength λ. Let the Cartesian coordinates of the scattering vector be $\mathbf{s} = (s_1, s_2, s_3)$. Then the transverse (i.e. equatorial) component of the scattering vector be defined $s_{12} = \sqrt{s_1^2 + s_2^2}$. The direction s_* of the quasi-meridional component depends on the studied material. In each cut the 110-peak is separated from its background resulting in the peak curves $I_{(110)}(s_{12})$ and $I^*_{(110)}(s_*)$, respectively. From the peak curves 1D reflection strengths

$$S_1 = \int I_{(110)}(s_{12})\, ds_{12}$$

and

$$S_1^* = \int I^*_{(110)}(s_*)\, ds_*$$

are integrated, which describe the trend of crystallinity evolution during the experiment. Additionally, 1D integral breadths

$$B_1 = \frac{S_1}{\max\left(I_{(110)}(s_{12})\right)}$$

and

$$B_1^* = \frac{S_1^*}{\max\left(I^*_{(110)}(s_*)\right)}$$

are computed, from which quantities $b_1 = 1/B_1$ and $b_1^* = 1/B_1^*$ are obtained that are used as measures for the lateral extension of the c-oriented and the a^*-oriented crystallites.[36] The required manual operations comprise proper rotation and background subtraction. They have to be carried out twice for each diffraction pattern. The processing of several thousand patterns collected in 1 day has been carried out in 3 months by 1 person.

3.2 The 3D WAXS Data Analysis

3D WAXS data analysis requires first to map[30,35,37,38] the recorded pattern from the detector plane into reciprocal space. During mapping the fiber rotation angle and the fiber tilt angle are automatically determined.[29] Thermal expansion of crystallites is not regarded. Thus, the distance of the tumbling sample from the detector is individually computed for each diffraction pattern from the tabulated[34] positions of the reflections of the α_2-modification of PP. After the mapping, the recorded diffraction data fill a nearly spherical volume (Fig. 2b) in reciprocal space except for a blind volume that extends along the meridian. Mapping of one pattern takes 2 s. The extraction and analysis of two 110-peaks requires 20 s for each pattern. Most of the machine time is spent in a 2D background extrapolation routine. The source code of the computer programs is freely available.[39] The core procedures are wf_spotana.pro and wf_merfit.pro.

After the fiber mapping even the quasi-meridional 110-reflection is always found at the same place. Thus, the manual effort is limited to the definition of two regions of interest (ROI) that are valid for all patterns in all experiments. In each of these regions a single peak is found. Before the analysis of the quasi-meridional peak the blind gap must be filled by extrapolated data (wf_merfit.pro). An algorithm based on radial basis functions[40] is applied, which returns a smooth background. Nevertheless, it is not capable to reconstruct the central reflection intensity (cf. Fig. 3). The error introduced by this shortcoming is discussed in the following section. Finally, each reflection spot is analyzed by the procedure wf_spotana.pro.

---

[2] E.g. $s_{12} = (2/\lambda)\sin(0.5\arctan(p_{12}/R))$ with R the sample-detector distance.

The analysis employs standard methods[41,42] of digital image processing. Application of the Sobel-operator localizes the reflection inside its ROI. The opening-operator makes sure that its center and the outer fall-off region are accounted for. The remnant pixels of the ROI are background. They are used for background extrapolation. The background is subtracted, and separated peaks $I_{(110)}(\mathbf{s})$ and $I^*_{(110)}(\mathbf{s})$ are obtained. For the computation of the total reflection intensities,

$$S = 2\pi \iint s_{12}\, I_{(110)}\left(s_{12}, s_3\right)\, ds_{12} ds_3,$$

and

$$S^* = 2\pi \iint s_{12}\, I^*_{(110)}\left(s_{12}, s_3\right)\, ds_{12} ds_3,$$

fiber symmetry is exploited. According to Ruland[43,44] these integrals are proportional to the weight crystallinity of the perfect crystals in the irradiated volume. Nevertheless, because a small fraction of the meridional intensity is invisible and not reconstructed, the determined value of S^* is somewhat too small.

For a determination of the radial integral breadth B first radial scattering curves of the extracted peak

$$I_{(110)}(s) = 2\pi \int s_{12} I_{(110)}(s, \phi)\, d\phi$$

are computed by azimuthal integration ($\cos\phi = s_{12}/s$). From $I_{(110)}(s)$

$$B \;=\; \int I_{(110)}(s)\, ds / \max\left(I_{(110)}(s)\right)$$

is obtained. Analogously, the breadth B^* of the a^*-oriented crystallites is computed. From the Fourier-transform breadth theorem[36] it follows that $b = 1/B$ and $b^* = 1/B^*$ are the integral breadths of the lateral extensions for the effective shape function of the crystallites with c-axis orientation and a^*-axis orientation, respectively. After crystallization has started, peaks are emerging out of the noisy background. The procedure can separate narrow peaks (e.g. a^*-set reflections) from the noise at already lower peak integrals than broader ones.

Although the shape function[36] of the crystallites comprises several factors, we are not trying to separate these factors but call the inverse integral breadths "minimum crystallite extension", instead. We consider this permitted in this study, because here the shape of the corresponding curves is used, first, to compare results of different data extraction methods, and, second, to detect remnant crystals in the early stage of crystallization after quenching from the rather cool melt. Thus, we do not discuss effects[36,45,46] that additionally broaden the reflections like the natural line width, strain broadening, and crystallite imperfections.

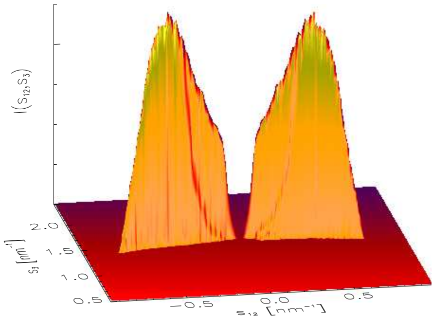

Figure 3: Typical quasi-meridional 110-peaks of HEPP as extracted (During recrystallization 24 min after quenching to 150°C). Displayed region: -1 nm^{-1}< s_{12} <1 nm^{-1}, 0.5 nm^{-1}< s_3 <2.5 nm^{-1}

Error upon Extraction of the Meridional Peak. A typical extracted meridional peak $I^*_{(110)}\left(s_{12}, s_3\right)$ is shown in Fig. 3. The observable ridge on the reflection is an artifact that is caused from inaccuracy of the automatic fiber mapping concerning center and rotation angle of the raw diffraction pattern. The central break-in is caused from improper extrapolation into the blind gap at the meridian. Although the computed total reflection intensity S^* is somewhat too small, the error is moderated by the fact that the missing intensity is close to the meridian, i.e. it is distributed on circles with low radius (cf. Fig. 2b). Thus, the intensity from the underestimated region is contributing with low weight only. In our experiments it appears more grave that the underestimation is a function of the varying tilt angle β. Underestimation becomes negligible whenever $\beta = \theta_{110}$ passes half the scattering angle of the probed meridional reflection, because in this moment the symmetrical reflection geometry[36] is realized.

4 Results and Discussion

4.1 Tracking of the Fiber Tilt-Angle Under Thermal Load

The studied uniaxially oriented film samples are softening and warping upon heating (cf. Fig. 1). Thus, considerable tumbling of the fiber axis in the small volume irradiated by the X-ray beam is expected. The fiber mapping procedure[29,30] is automatically tracking both the fiber rotation and the tilt angle β. Based on these parameters the data are corrected. The statistical error of the tilt-angle determination can be estimated from the statistical noise on the tilt-angle curve $\beta(t)$ of the experiments.

In two of the 8 experiments carried out, $\beta(t)$ stays close to 0^{o}. In two other experiments extreme changes are observed. The corresponding curves are documented in Fig. 4 and Fig. 5. Figure 4 shows $\beta(t, T)$ of an experiment, in which very good signal-to-noise ratio in the patterns has been achieved by exposing for 20 s (cycle time:

30 s). The tracking curve appears rather smooth demonstrating the reliability of the tilt-angle determination. Figure 5 documents the most extreme tilt-angle variation from the experiments with 4 s exposure (8 s cycle time). The increased noise on the tracking curve is a result of the inferior signal-to-noise ratio in the diffraction patterns.

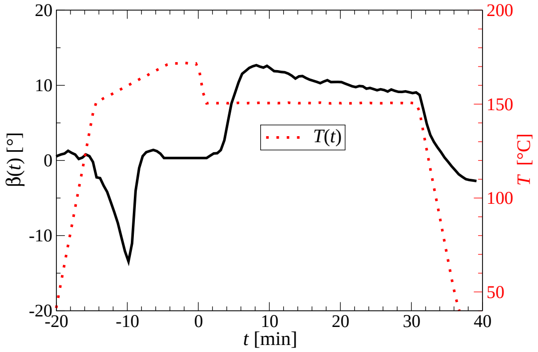

Figure 4: Tilt-angle tracking curve $\beta(t,T)$ from the automatic fiber-mapping procedure in an experiment with long exposure of the patterns (20 s), in which β is changing considerably (HEPP; melt-annealing at 171°C and recrystallization at 150°C)

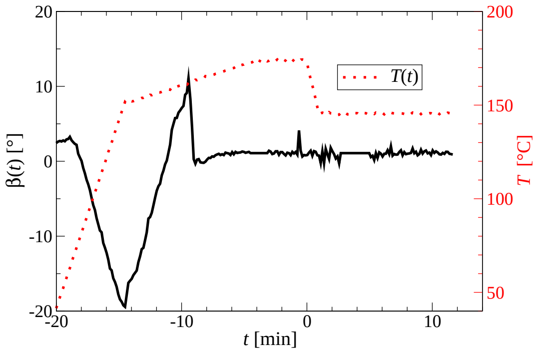

Figure 5: Tilt-angle tracking curve $\beta(t,T)$ from the automatic fiber-mapping procedure in an experiment with short exposure of the patterns (4 s), in which β is changing considerably (HEPP; melt-annealing at 173°C and recrystallization at 145°C)

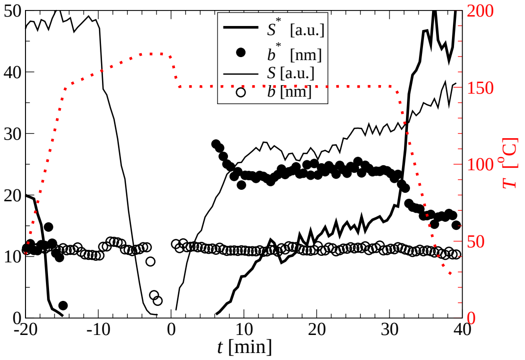

Figure 6: 3D analysis of the 110-reflections of HEPP under thermal load. Melting at 171°C and isothermal crystallization at 150°C. The dotted curve shows the temperature $T(t)$. Solid lines: Peak integrals in reciprocal space, S, and S^* of c-oriented and a^*-oriented crystals, resp. Symbols: Minimum lateral crystallite sizes (integral breadths) b and b^*

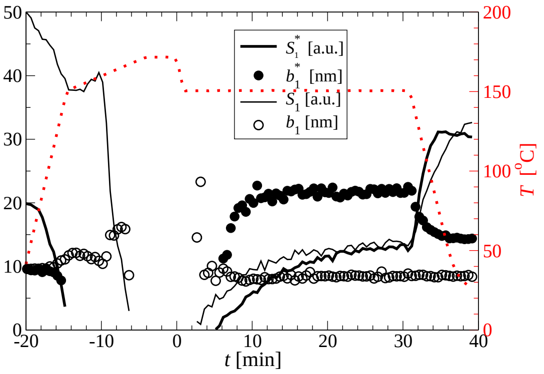

Figure 7: 1D analysis of sections cut through the 110-reflections of HEPP under thermal load. Melting at 171°C and isothermal crystallization at 150°C. The dotted curve shows the temperature $T(t)$. Solid lines: Peak strengths from the sections, S_1, and S_1^* of c-oriented and a^*-oriented crystals, resp. Symbols: Lateral crystallite sizes b_1 and b_1^*

4.2 Isothermal Crystallization at 150°C

Exactly as in a previous SAXS study[15] the HEPP sample has been melt-annealed at a furnace temperature of 171°C for 4 min and quenched to 150°C for isothermal crystallization. Figure 6 exhibits the results of the 3D reflection analysis in reciprocal space. Figure 7 shows the respective curves from the 1D WAXS trend analysis. Comparison of the two figures demonstrates that the essential features are recognized in both kinds of evaluation: Early melting and late crystallization of the a^*-oriented set become apparent both in the 1D-integrated peak intensity $S_1^*(t)$ and in the 3D-integral in reciprocal space, $S^*(t)$. Also the doubling of the size b^* of the a^*-set crystallites during crystallization from the quiescent melt is demonstrated in both analyses. Similarly, both evaluations show that the amount of the a^*-crystallites is considerably increasing during the quench after the isothermal phase (for $t > 30\,\text{min}$), but that the new crystallites do not grow big.

On the contrary, the evaluation of sections $S_1(t)$ pretends for $t > 30\,\text{min}$ a steep increase of the c-crystallites, whereas the weight-crystallinity $S(t)$ is increasing only gradually. Interpretation of the integral crystallite sizes b^* yields that the first a^*-crystallites appear to be big ones. On the contrary, the simple 1D analysis (b_1^*) suggests that the first a^*-oriented crystallites were small. For the other studied experiments both the general agreement and the individual discrepancies of the 1D and the 3D method are similar.

Remanent Crystal Nuclei. In Fig. 6 the trend of the strength $S(t,T)$ close to $t = 0$ is indicative for remanent nuclei of the c-set. For other (not presented) experiments with a melt-annealing temperature of 171°C remanent crystal reflections have even been observed. Thus, in a second series of experiments the melt-annealing temperature is increased to 173°C. The time-resolution is enhanced (8 s cycle time) on the expense of background noise. The amount of collected data is kept low by lowering the interval in which WAXS-monitoring is turned on. Figure 8 shows the result for the crystallization at 150°C. A latency period of about 10 min that can now be read from the peak-integral curves confirms the suspicion. Nuclei must have been present after quenching from the cooler melt, although in the earlier SAXS study[15] a measured furnace temperature of 171°C had proven sufficient.

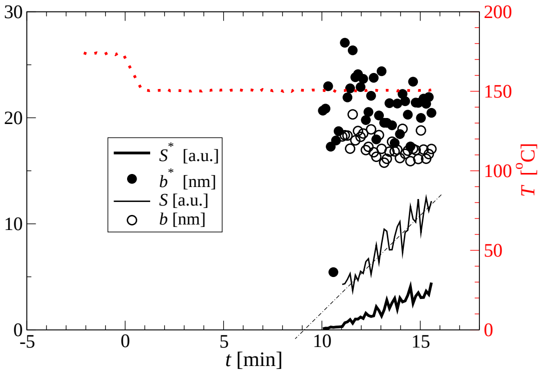

Figure 8: 3D analysis of the 110-reflections of HEPP under thermal load. Melting at 173°C and isothermal crystallization at 150°C. The dotted curve shows the temperature $T(t)$. Solid lines: Peak integrals in reciprocal space, S, and S^* of c-oriented and a^*-oriented crystals, resp. Symbols: Lateral crystallite sizes (integral breadths) b and b^*

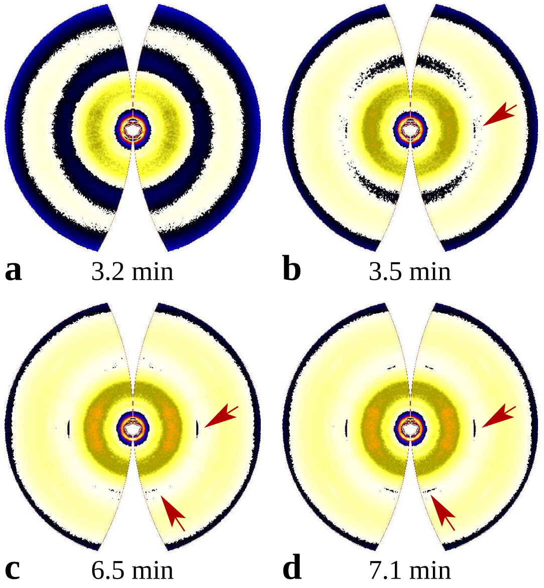
a 3.2 min **b** 3.5 min

c 6.5 min **d** 7.1 min

Figure 9: Visual inspection of the crystalline reflections of HEPP under thermal load. Isothermal crystallization after melting at 173°C. Indicated is the time after quenching to 150°C

In many studies, WAXS patterns are not analyzed by peak integration, but by visual inspection. Figure 9 shows mapped diffraction patterns in a pseudo-color intensity scale that brings out even weak reflections in print. 3.2 min after the quench (Figure 9a) only an isotropic amorphous halo is observed. Thus, visual inspection and peak integration are still in agreement. Already after 3.5 min (Fig. 9b) the amorphous halo has somewhat retracted from the equator, where now a weak 110-reflection is perceptible. The first indication of a^*-oriented crystallites is found after 6.5 min (Fig 9c), and is clearly visible after 7 min. Throughout the interval covered in Fig. 9, the 3D-peak analysis does not return a significant integral. The corresponding weight crystallinity is still very small.

Assuming that the weight-crystallinity of the completely crystallized material is 50% ± 20%, the comparison of the low and the high end of the peak-strength curves shows that the automatic peak-analysis logs in at weight-crystallinities that are close to 1%. The fact that reflections are visually conceivable long before that threshold is surpassed indicates that relevant weight-crystallinities (in the sense of materials science) are generated much later than visual inspection presumes. The evolution of crystallinity is discussed in Section 4.5.

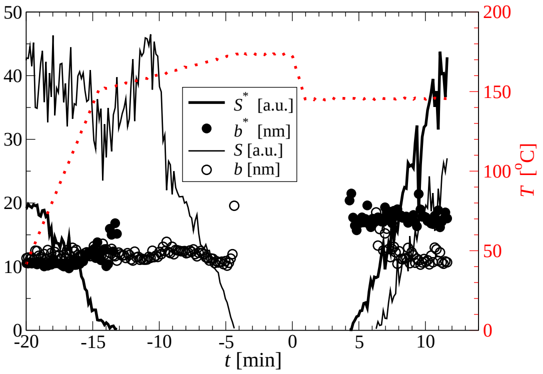

Figure 10: 3D analysis of the 110-reflections of HEPP under thermal load. Melting at 173°C and isothermal crystallization at 145°C. The dotted curve shows the temperature $T(t)$. Solid lines: Peak integrals in reciprocal space, S, and S^* of c-oriented and a^*-oriented crystals, resp. Symbols: Lateral crystallite sizes (integral breadths) b and b^*

4.3 Isothermal Crystallization at 145°C

Figure 10 shows the evolution of crystallites during melting and crystallization. The automatic peak analysis is catching the strength $S^*(t)$ of the a^*-set 4 min after the quench. $S(t)$ starts 6 min after quenching to 145°C.

Again, the peaks are detected earlier by visual inspection. 3.1 min after quenching (Fig. 11a) the material is still completely amorphous. 8 s after that (Fig. 11b) both the quasi-meridional 110-reflection of the a^*-set, and the 131-reflection is visible. At $t = 3.5$ min (Fig. 11d) even the equatorial 110-peaks are observable. In HEPP crystallized isothermally at 145°C from the quiescent melt, the a^*-oriented crystallites appear earlier than the c-crystallites.

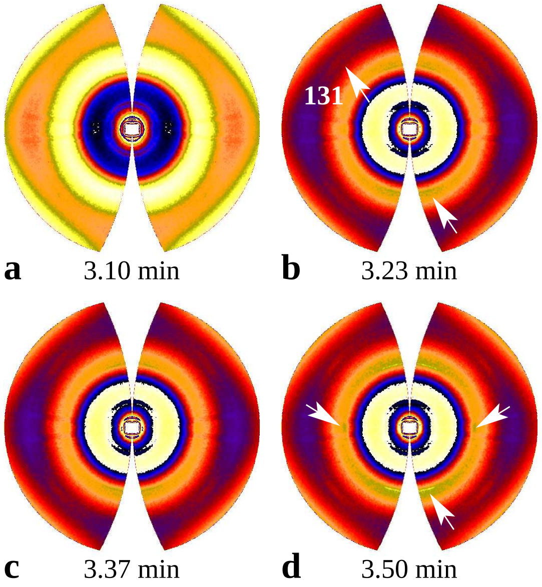

Figure 11: Visual inspection of the crystalline reflections of HEPP under thermal load. Isothermal crystallization after melting at 173°C. Indicated is the time after quenching to 145°C. The horizontal distortion in the center is resulting from adhesive tape holding the beam stop

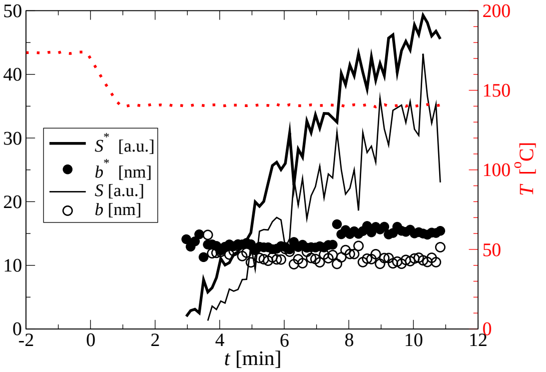

Figure 12: 3D analysis of the 110-reflections of HEPP under thermal load. Melting at 173°C and isothermal crystallization at 140°C. The dotted curve shows the temperature $T(t)$. Solid lines: Peak integrals in reciprocal space, S, and S^* of c-oriented and a^*-oriented crystals, resp. Symbols: Lateral crystallite sizes (integral breadths) b and b^*

4.4 Isothermal Crystallization at 140°C

Figure 12 shows the evolution after the quench from 173°C to 140°C. The process is faster than at 145°C. Now the quasi-meridional peaks of the a^*-set become separable after 3 min. The equatorial c-set reflection is first captured after 3.5 min. The minimum extensions b and b^* of both kinds of crystallites are almost identical in the beginning. 7.5 min after the quench, b^* jumps up from 12 nm to 15 nm. Again, the eye detects the crystalline reflections earlier. Figure 13a shows after 1.5 min still an amorphous melt. 16 s later (Fig. 13b) both the reflection on the first layer line (arrow labeled "131"), and the quasi-meridional a^*-related reflection becomes visible. It takes another 40 s before the c-set crystallites are distinguished (Fig.13d). Here even all 3 strong equatorial reflections of PP show up simultaneously.

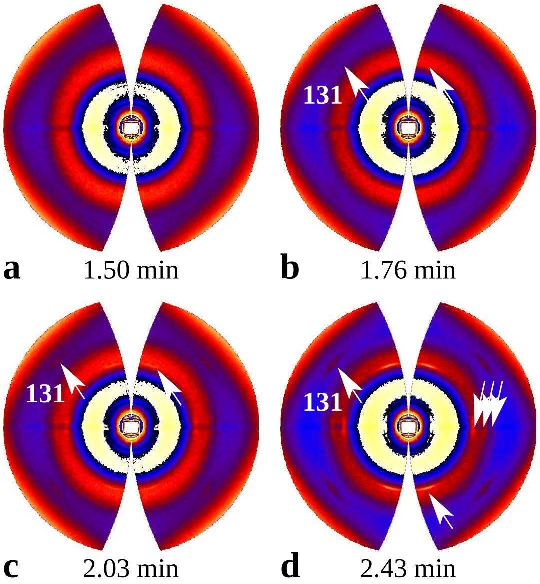

Figure 13: Visual inspection of the crystalline reflections of HEPP under thermal load. Isothermal crystallization after melting at 173°C. Indicated is the time after quenching to 140°C. The horizontal distortion in the center is resulting from adhesive tape holding the beam stop

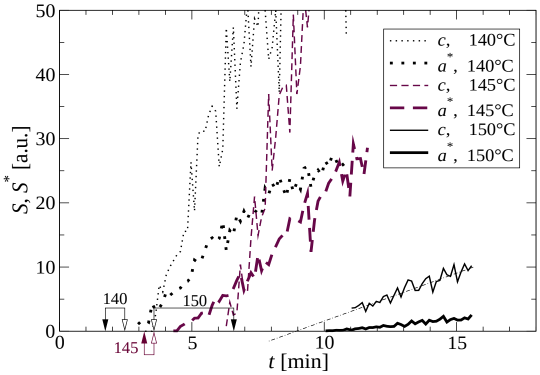

Figure 14: Evolution of relative weight crystallinities of the a^*-oriented crystallites (bold lines) and of the c-oriented crystallites (thin lines) during isothermal, oriented crystallization of HEPP from a quiescent melt as a function of crystallization temperature. Double-arrows indicate the first sighting of the a^*-set (full arrow head), and of the c-set (open arrow head), respectively

4.5 Evolution of weight crystallinities

Figure 14 shows the evolution of the weight crystallinities of the two sets of crystallites at the 3 different crystallization temperatures. In this plot all 3D peak-integral curves are normalized in the same way. Thus, they can be compared relative to each other. As shown by Ruland,[43] such reflection integrals that are complete in reciprocal space are proportional to the weight crystallinity of the perfect crystallites that cause the reflections.

Latency periods. In Fig. 14 visually determined latency periods between the beginning of the quench and the first observation of 110-reflections are indicated by double-head arrows. Full arrow heads mark t_{v0}^*, i.e. the first sighting of the quasi-meridional reflection of the a^*-oriented crystallite set. The open head indicates t_{v0}, i.e. the first observation of the equatorial reflection.

Latency periods t_0^* and t_0 determined from the weight-crystallinity curves are defined by the conditions $S^*(t_0^*) = 0$ and $S(t_0) = 0$, respectively. At the crystallization temperature T_c =150°C the value $t_0 = 9$ min must be extrapolated (dashed-dotted line), because the separation algorithm captures the peak rather late. Both kinds of latency periods are increasing in similar manner as a function of T_c. At low T_c (140°C) the latency periods of the a^*-set are shorter than that of the c-set. With increasing T_c both t_{v0}^* and t_0^* are increasing more rapidly than t_{v0} and t_0. Finally, at T_c =150°C, the latency of the c-set has become shorter than that of the a^*-set.

The figure shows that always $t_{v0} < t_0$ and $t_{v0}^* < t_0^*$ is valid. The difference is considerable. It is significant, because the peak-integration algorithm logs in at very low weight crystallinities for most of the peaks, and no steepening of the curves is observed close to the end of the latency periods (the opposite is observed during second melting – cf. Fig. 16 and the corresponding discussion).

Because in the intervals $[t_{v0}, t_0]$ and $[t_{v0}^*, t_0^*]$ the weight-crystallinity is increasing much more slowly than thereafter, we propose that here a crystallization mechanism of its own is active, which is dominated by equilibrium between wax and wane of crystallites. This means that, in fact, we are observing nuclei. If a critical density of nuclei would induce the growth of stable crystals, the average distance between the nuclei would become the average distance between Strobl's blocks.[27,28]

Crystallization velocities. The slopes of the curves from Fig. 14 are proportional to the crystallization velocities and can be compared with respect to each other. The graphs exhibit the well-known fact that all velocities slow down as the undercooling is decreasing. Moreover, the initial velocity of the a^*-set crystallites is less than half of the velocity of the c-set crystallites.

4.6 Combining WAXS and SAXS Results

In the following discussion we assume that the sample temperature curves in the WAXS experiments are sufficiently close to those in the SAXS experiments. In the isotropic and shear-induced studies on polypropylene crystallization cited in the introduction, similar latency periods and general features are reported as a function of crystallization temperature. Nevertheless, only combined SAXS-WAXS experiments with 2D detectors and high time resolution will help to remove the uncertainty.

4.6.1 Crystallization at 150°C

In the SAXS study (,[15] Fig. 5) strong meridional scattering has been detected in the first minutes, from which equatorial scattering begins to grow first slowly ($t > 4$ min), later ($t > 10$ min) more rapidly. Because we and others[9,17] do not observe any discrete WAXS for $t < 9$ min, the strong meridional streak must be related to a layer-shaped modulation of the electron density in an amorphous melt. The axis of the layer stack is parallel to the fiber axis. At the beginning of the equilibrium-dominated crystallization, these layers are populated by latent crystallites of first the c-set, second the a^*-set. Weak equatorial scattering indicates lateral correlation among the crystallites. The 3D peak integrals demonstrate that meaningful weight fractions of crystallites are not available for t <9 min. Thus, there is no material to build a cross-hatched topology that could be responsible for the equatorial scattering that is observed for 4 min< t <9 min in the SAXS study (,[15] Fig. 5). Unfortunately, the meridional streak of the decomposed melt is dominating the SAXS and thus, a quantitative analysis is impossible.

Only at this high crystallization temperature the few a^*-crystallites growing from the quiescent melt may be addressed "daughter"[26] crystallites, because they start later than the c-crystallites. Anticipating some of the results obtained for lower crystallization temperatures our notion of the shallow-quench crystallization is sketched in Fig. 15.

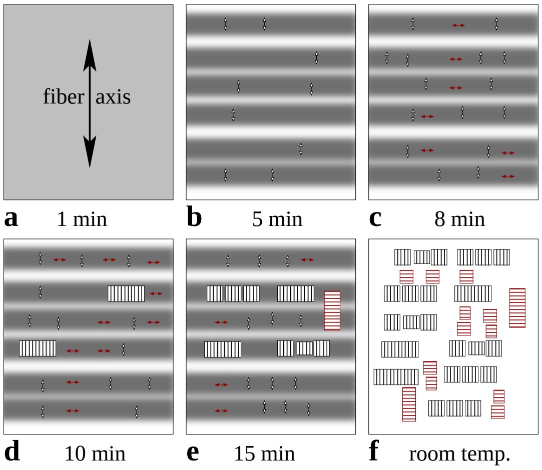

Figure 15: HEPP crystallizing from a quiescent, oriented melt at 150°C. a) homogeneous melt b) decomposed melt with c-set nuclei (blocks) c) melt with c-set and a^*-set nuclei d) primary c-set lamella e) c-set and primary a^*-set lamellae f) cross-hatched structure

4.6.2 Crystallization at 145°C

In the SAXS study[15] the analysis of the patterns recorded during the first 3 min had only detected row assemblies[19,26] of nuclei. In this period the WAXS shows a completely amorphous material. In the interval $3\,\mathrm{min} < t < 4.5\,\mathrm{min}$ the WAXS exhibits the equilibrium-dominated regime of the crystallization. Here the SAXS (,[15] Fig. 9) detects a stable block structure of mid-range correlation both in fiber direction and in lateral direction. For $t > 4.5\,\mathrm{min}$ the WAXS peak-integral curves $S(t)$ and $S^*(t)$ indicate the growth-dominated regime of the crystallization. During this period the evolution of the SAXS has been interpreted by a merging of the blocks into lamellae. Taking into account the evolution of $S(t)$ and $S^*(t)$, also a different interpretation would yield the same evolution of the SAXS. For this interpretation it is sufficient to assume that two sets of differently oriented (block-shaped) nuclei are populating the melt and start to grow into lamellae. As the faster c-lamellae overtake the earlier but slower a^*-lamellae, the evolution of the SAXS suggests a merging of a c-set block structure into lamellae. This is a classical growth-from-nuclei mechanism that is generating two differently oriented sets of layer-shaped domains that do not take notice of each other.

4.6.3 Crystallization at 140°C

In the SAXS study[15] a clear evolution of domain structure has only been observed during the period up to $t = 3\,\mathrm{min}$. According to the WAXS, here the growth-dominated crystallization is starting. A detailed description of the nanostructure evolution has been impossible, because the time-resolution has been insufficient for the fast process. Thus, the period before the start of the nucleation (equilibrium-dominated crystallization) has not been resolved by the SAXS. The SAXS recorded during the regime of equilibrium-dominated crystallization has shown a 3D arrangement (,[15] Fig. 7) of blocks (i.e. nuclei) that turn from an entwined arrangement into a checkered arrangement while at the same time the gaps between the blocks are shrinking both in lateral and in longitudinal direction. Because the WAXS shows that there is not much increase of crystallinity, the SAXS results could be explained by the notion that during the equilibrium-dominated crystallization the amplitude of the size-fluctuation of the nuclei appears to be increasing. The following growth-dominated phase has shown a constant SAXS pattern with increasing discrete intensity that has been interpreted as a dynamic equilibrium in which crystallites are emerging and ripening.

4.6.4 Crystallization temperature and Crystallization Mechanisms

In summary, the combined results of SAXS and WAXS show that the dominance of the involved crystallization mechanisms can be adjusted by variation of the crystallization temperature.

Only upon shallow quench a decomposition of the melt into oriented layers of different electron density is clearly the first mechanism. The first nuclei observed in the structured melt are belonging to the c-oriented set. Nuclei of the a^*-set appear somewhat later. Growth of stable crystallites starts considerably later.

At medium quench depth decomposition is not observed. Only row assemblies[19,26] are found[15] in the melt. After transition into the nucleation phase the SAXS shows an arrangement of blocky crystallites. During the growth-dominated phase the SAXS evolution can be described by merging of blocks or by a bimodal structure of differently oriented blocks that are growing and forming lamellae.

Deep quench causes very early nucleation. Again, the a^*-set is nucleated first. As the growth-phase is starting, the structure is replicated all over the volume and a superposition of structures in different states after induction is observed. Because of this dynamic equilibrium it is impossible to separate late crystallization mechanisms.

4.7 Melting Mechanisms

Already in our SAXS study[15] we had detected a sequence of several melting mechanisms in the industrial HEPP. In the temperature range until 158°C we had observed the melting of secondary lamellae that are less extended in equatorial direction. Now the WAXS data (Figures 6 and 10) exhibit that these domains are containing the a^*-oriented crystallites. This result is in agreement with several studies[3,5,26,47] in which a^*-oriented crystallites generated under extensional flow conditions were found to be of secondary nature.

For $158^{\mathrm{o}}\mathrm{C} < T < 162^{\mathrm{o}}\mathrm{C}$ the SAXS study had exhibited a considerable decrease of the average lateral extension of the lamellae, and an increase of the average long period had been found. This mechanism had been interpreted as the melting of extended secondary lamellae. In this temperature interval the WAXS data show that the weight crystallinity of perfect crystallites with normal chain orientation ($S(t,T)$) is only subject to little change (Figures 6 and 10). This finding can be explained by recrystallization, i.e. the melting of crystallites inside imperfect lamellae that is superimposed by crystallization of distorted zones inside these secondary lamellae.

For $T > 162^{\mathrm{o}}\mathrm{C}$ the SAXS study[15] had shown a third melting mechanism: “The long period remains almost constant and the average layer extension is increasing, indicating the melting of (now the primary) crystalline lamellae with the less extended layers melting first”. Also the WAXS data exhibit a third mechanism. At 162°C the weight crystallinity of the c-set falls off abruptly. Thereafter it is decreasing more slowly following a sigmoidal course until it reaches the value zero. This finding is in agreement with the explanation given in the SAXS study.

The weight of the crystallites inside the secondary lamellae decreases abruptly, as soon as they are no longer nourished from the distorted zones. Thereafter the primary lamellae melt from edge to core, and the sigmoidal decay is caused from the size distribution of the primary lamellae. Thus, these primary lamellae of the *c*-set appear to be grown from nuclei.

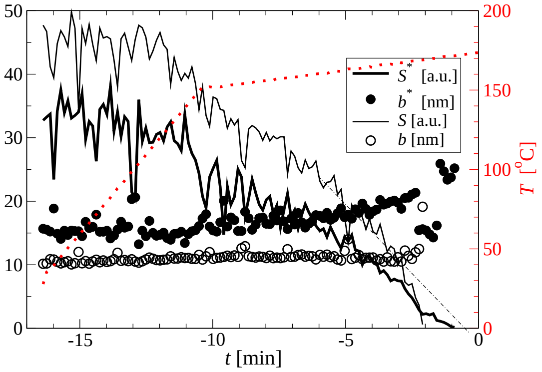

Figure 16: 3D analysis of the 110-reflections of HEPP under thermal load. Second melting after an isothermal crystallization experiment. The dotted curve shows the temperature $T(t)$. Solid lines: Peak integrals in reciprocal space, S, and S^* of *c*-oriented and a^*-oriented crystals, resp. Symbols: Lateral crystallite sizes (integral breadths) b and b^*

4.8 Second Melting

As had been done in our SAXS study,[15] we have molten the samples after the crystallization experiment for a second time. Figure 16 shows the result for the sample that had been crystallized at 145°C before. After the crystallization experiment, the minimum lateral extension b^* of crystallites in a^*-orientation is much larger than in the industrial HEPP (cf. Fig. 6, Fig. 10). Here the a^*-set crystallites show a very similar melting behavior as the *c*-set crystallites. The apparently somewhat earlier melting ($t_{0m} < t^*_{0m}$ with $S(t_{0m}) = 0$, $S^*(t^*_{0m}) = 0$) of the *c*-set crystallites is not considered significant. The *c*-set 110-reflection is much broader than the quasi-meridional reflection of the recrystallized a^*-set. Close to its disappearance it is more difficult for the peak-extraction procedure to separate the *c*-set reflection from the noise than it is for the sharp a^*-set reflection. In case of the anticipated systematic deviation, the fall-off of the determined curve $S(t)$ should considerably increase before it vanishes, because the tails of the reflection drown in the noise. The difference between the extrapolation line shown in Fig. 16 and the measured curve is indicative for such an effect. In summary, the material recrystallized from the quiescent melt exhibits a simple melting mechanism which is very similar for both the differently oriented crystallite sets.

5 Conclusion

Variation of process parameters causes considerable variation of the crystallization mechanisms and the resulting nanostructure of polypropylene. There is no simple general crystallization mechanism. This is not only demonstrated by the differences among the materials monitored at different crystallization temperatures, but in particular after comparing these results to the structure and the melting mechanisms found in the commercial starting material (hard-elastic polypropylene). Obviously, evolution mechanisms observed under isothermal conditions in a quiescent melt cannot be simply transferred to the behavior of polymer melts crystallizing under gradients of temperature and pressure that are typical for industrial processes.

It is generally reported that the *c*-set crystallites are formed during primary crystallization, whereas the a^*-oriented crystallites are of secondary nature ("daughter lamellae", "cross-hatched lamellae").[3,26,47] Our results demonstrate that this may not be the case for a crystallization from an oriented quiescent melt. Upon deep quench, crystallization is starting in the a^*-set. In contrast, the industrial process in which the HEPP-material is produced, obviously is governed by the commonly reported sequence. In the commercial material the reflections of the a^*-set crystallites are much broader than after recrystallization, and the small a^*-set crystallites of HEPP are melting at much lower temperature than the *c*-set crystallites.

Application of the new automatic method for the computation of 3D peak-integrals in reciprocal space has resulted in plots demonstrating that crystallite formation is a two-stage process. It is observed both in the homogeneous and in the decomposed melt (i.e. deep and shallow quench). In the first stage there is little increase of the very low crystallinity, until crystallinity starts to grow rapidly in the second stage. Thus, the historical discussion concerning the sensitivity[9,11–13] of WAXS detectors appears to be settled for oriented samples: Even the available standard detectors register WAXS reflections already in the first stage in which the crystallinity remains that low that it does not yet contribute to the SAXS. In our experiments we have not observed rigid stable shish-kebab nuclei that have recently been observed in the group of Hsiao[48] with polyethylene and that should not melt[49] under the mild melting conditions chosen by us. After the combination of the older SAXS results with the new WAXS data, the shallow-quench meridional streak in the SAXS appears no longer related to crystalline lamellae, but to a decomposed melt. The same has been found with polyethylene.[14,50] It looks as if in particular the layer-arrangement mechanism of "random car parking"[51–53] is not characterizing crystallization itself, but a precedent decomposition of the melt. A possible explanation for the fact that decomposition is not detected in some studies of isotropic PP crystallization may be related to a combination of chemical composition, sample history, quench depth, solid-angle average of the SAXS, background subtraction, and definition of the zero-time.

Admittedly, the combination of results from *successively* executed SAXS and WAXS experiments is of limited significance, as long as the exact temperature in the irradiated volume of the sample cannot be measured. Simultaneous measurements of anisotropic scattering that provide complete patterns for quantitative analysis will not be possible, until detectors with a central hole and electronic read-out become available. A detector device that is assembled from tiles[54] might be adaptable by omitting a central tile.

Acknowledgments. The authors thank J.C. Gregor for carrying out the 1D-WAXS trend analysis and the Hamburg Synchrotron Radiation Laboratory (HASYLAB) for beam time granted in the frame of project II-04-039. We gratefully acknowledge funding by the Deutsche Forschungsgemeinschaft, project STR 501/4-2. Part of this work has been supported by the 7th framework program of the European Union (Project NANOTOUGH FP7-NMP-2007-LARGE)

References

(1) Compostella, M. Coen, A. Bertinotti, F.; *Angew. Chem.* **1962**; *74*, 618.
(2) Clark, E. S. Spruiell, J. E.; *Polym. Eng. Sci.* **1976**; *16*, 176.
(3) Katayama, K. Amano, T. Nakamura, K.; *Kolloid Z. Z. Polym.* **1968**; *226*, 125.
(4) Norton, D. R. Keller, A.; *Polymer* **1985**; *26*, 704.
(5) Olley, R. H. Bassett, D. C.; *Polymer* **1989**; *30*, 399.
(6) Li, H. Sun, X. Wang, J. Yan, S. Schultz, J. M.; *J. Polym. Sci. Part B Polym. Phys.* **2006**; *44*, 1114.
(7) Albrecht, T. Strobl, G.; *Macromolecules* **1995**; *28*, 5267.
(8) Ryan, A. J. Terrill, N. J. Fairclough, J. P. A.; *ACS Symp. Ser.* **2000**; *739*, 201.
(9) Heeley, E. L. Maidens, A. V. Olmsted, P. D. Bras, W. Dolbnya, I. P. Fairclough, J. P. A. Terrill, N. J. Ryan, A. J.; *Macromolecules* **2003**; *36*, 3656.
(10) Dai, P. S. Cebe, P. Capel, M. Alamo, R. G. Mandelkern, L.; *J. Appl. Cryst.* **2000**; *33*, 714.
(11) Wang, Z.-G. Hsiao, B. S. Sirota, E. B. Agarwal, P. Srinivas, S.; *Macromolecules* **2000**; *33*, 978.
(12) Panine, P. Urban, V. Bösecke, P. Narayanan, T.; *J. Appl. Cryst.* **2003**; *36*, 991.
(13) Panine, P. Di Cola, E. Sztucki, M. Narayanan, T.; *Polymer* **2008**; *49*, 676.
(14) Stribeck, N. Almendarez Camarillo, A. Cunis, S. Bayer, R. K. Gehrke, R.; *Macromol. Chem. Phys.* **2004**; *205*, 1445.
(15) Stribeck, N. Nöchel, U. Almendárez Camarillo, A. Roth, S. V. Dommach, M. Bösecke, P.; *Macromolecules* **2007**; *40*, 4535.
(16) Somani, R. H. Hsiao, B. S. Nogales, A. Srinivas, S. Tsou, A. H. Sics, I. Baltá Calleja, F. J. Ezquerra, T. A.; *Macromolecules* **2000**; *33*, 9385.
(17) Somani, R. H. Yang, L. Hsiao, B. S. Agarwal, P. K. Fruitwala, H. A. Tsou, A. H.; *Macromolecules* **2002**; *35*, 9096.
(18) Somani, R. H. Yang, L. Hsiao, B. H. Fruitwala, H.; *J. Macromol. Sci. Part B Phys.* **2003**; *B42*, 515.
(19) Nogales, A. Mitchell, G. R.; *Polymer* **2005**; *46*, 5615.
(20) Ogino, Y. Fukushima, H. Takahashi, N. Matsuba, G. Nishida, K. Kanaya, T.; *Macromolecules* **2006**; *39*, 7617.
(21) Elias, H.-G.; *Polymere: Von Monomeren und Makromolekülen zu Werkstoffen*; Zug: Hüthig und Wepf; **1996**.
(22) Suaphol, P. Lin, J.-S.; *Polymer* **2001**; *42*, 9617.
(23) Cho, K. Saheb, D. N. Choi, J. Yang, H.; *Polymer* **2003**; *43*, 1407.
(24) De Rosa, C. Ruiz de Ballesteros, O. Di Gennaro, M. Auriemma, F.; *Polymer* **2003**; *44*, 1861.
(25) Xu, J. Srinivas, S. Marand, H. Agarwal, P.; *Macromolecules* **1998**; *31*, 8230.
(26) Kumaraswamy, G. Verma, R. K. Issaian, A. M. Wang, P. Kornfield, J. A. Yeh, F. Hsiao, B. S. Olley, R. H.; *Polymer* **2000**; *41*, 8931.
(27) Hugel, T. Strobl, G. Thomann, R.; *Acta Polym.* **1999**; *50*, 214.
(28) Strobl, G.; *Progr. Polym. Sci.* **2006**; *31*, 398.
(29) Stribeck, N.; *Acta Cryst.* **2009**; *A65*, 46.
(30) Stribeck, N. Nöchel, U.; *J. Appl. Cryst.* **2009**; *42*, in print.
(31) Noether, H. D.; *Intern. J. Polymeric Mater.* **1979**; *7*, 57.
(32) Sprague, B. S.; *J. Macromol. Sci. Phys.* **1973**; *B8*, 157.
(33) Noether, H. D. Whitney, W.; *Colloid Polym. Sci.* **1973**; *251*, 991.
(34) Mencik, Z.; *J. Macromol. Sci. Phys.* **1972**; *B6*, 101.
(35) Polanyi, M.; *Z. Phys.* **1921**; *7*, 149.
(36) Stribeck, N.; *X-Ray Scattering of Soft Matter*; Heidelberg, New York: Springer; **2007**.
(37) Fraser, R. D. Macrae, T. P. Miller, A. Rowlands, R. J.; *J. Appl. Cryst.* **1976**; *9*, 81.
(38) Millane, R. P. Arnott, S.; *J. Macromol. Sci. Phys.* **1985**; *B24*, 193.
(39) Stribeck, N.; *Downloads*; http://www.chemie.uni-hamburg.de/tmc/stribeck/dl; **2008**.
(40) Buhmann, M. D.; *Acta Numerica* **2000**; *9*, 1.
(41) Haberäcker, P.; *Digitale Bildverarbeitung*; Munich: Hanser; **1989**.
(42) VNI; *PV-WAVE manuals*; V 7.5, Boulder, Colorado; **2007**.
(43) Ruland, W.; *Acta Cryst.* **1961**; *14*, 1180.
(44) Alexander, L. E.; *X-Ray Diffraction Methods in Polymer Science*; New York: Wiley; **1979**.
(45) Warren, B. E.; *X-Ray Diffraction*; New York: Dover;

1990.

(46) Guinier, A.; *X-Ray Diffraction*; San Francisco: Freeman; **1963**.

(47) Sakthivel, A. Abhiraman, S.; *J. Appl. Polym. Sci.* **1984**; *29*, 4257.

(48) Keum, J. K. Zuo, F. Hsiao, B. S.; *Macromolecules* **2008**; *41*, 4766.

(49) Janeschitz-Kriegl, H. Eder, G.; *J. Macromol. Sci. Phys.* **2007**; *46*, 591.

(50) Stribeck, N. Almendarez Camarillo, A. Nöchel, U. Bösecke, P. Bayer, R. K.; *Anal. Bioanal. Chem.* **2007**; *387*, 649.

(51) Rényi, A.; *Sel. Transl. Math. Stat. Prob.* **1963**; *4*, 203.

(52) Schultz, J. M. Lin, J. S. Hendricks, R. W.; *J. Appl. Cryst.* **1978**; *11*, 551.

(53) Stribeck, N.; *Macromol. Chem. Phys.* **2004**; *205*, 1455.

(54) Broennimann, C. Eikenberry, E. F. Henrich, B. Horrisberger, R. Hülsen, G. Pohl, E. Schmitt, B. Schulze-Briese, C. Suzuki, M. Tomizaki, T. Toyokawa, A. Wagner, A.; *J. Synchrotron Rad.* **2006**; *13*, 120.